A R C H I V E O F M E C H A N I C A L E N G I N E E R I N G

Volume 66 2019 Number 3

DOI: 10.24425/ame.2019.129679

Key words: development of fatigue crack, crack flexibility, directional (full) spectrum, higher harmonics, forward and backward whirl

Shravankumar C.,[1] Rajiv Tiwari[1]

Experimental identification of cracked rotor system parameters from the forward and backward whirl responses

In the present work, an experimental investigation of a transverse fatigue crack has been carried out. A mathematical modelling of cracked rotor system along with the measured vibration is used to find crack parameters that not only detect the fault but also quantify it. Many experimental studies on cracks considered the crack as a slit or notch, which remains open. However, such flaws do not mimic a fatigue crack behavior, in which crack front opens and closes (i.e., breathes in a single revolution of the rotor). The fatigue crack in rotors commonly depicts 2× frequency component in the response, as well as higher frequency components, such as 3×, 4× and so on. In rotors, both forward and backward whirling take place due to asymmetry in rotor, and thus the fatigue crack gives the forward and backward whirl for all such harmonics. A rotor test rig was developed with a fatigue crack in it; rotor motions in two orthogonal directions were captured from the rig at discrete rotor angular speeds using proximity probes. The directional-spectrum processing technique has been utilized to the measured displacements to get its forward and backward whirl components. Subsequently, it is executed in a mathematical model-based estimation procedure to obtain the crack forces, residual unbalances, and remaining rotor system unknown variables. Estimation of crack forces during rotation of the shaft gives its characteristics, which can be used further to develop newer crack models.

1. Introduction

In rotating machinery, the development of fatigue cracks is natural due to fatigue loading and its effect is disastrous. Ishida documented industrial rotor failures due to cracks and they occurred as early as in 1950s [1]. This demands

✉ R. Tiwari, e-mail: rtiwari@iitg.ac.in

[1]Department of Mechanical Engineering, Indian Institute of Technology Guwahati, Guwahati – 781039, India.

the fatigue crack identification in a rotor shaft as early as possible. Resources existing on identification of cracked rotors can be generally classified as: the mathematical model basis, vibration signature basis, experimental modal analysis and contemporary signal analysis [2]. Recently mathematical model basis procedures have been popular among researchers [3–5]. Investigation of test rigs with crack rotors is limited and mainly focused on a slit or notch. It does not simulate the breathing phenomenon of a fatigue crack. In this section, a brief review on the experimental methods used for the detection and diagnosis of cracks is provided.

Crack inhalation behavior was experimentally studied in [6] for the slit and fatigue cracks, and concluded that reduction in natural frequencies with crack size is higher in the former as compared to the latter type of crack. Through excitation method the coupling of different vibration modes (bending and axial) due to crack in a beam were studied in [7]. Similarly, the coupling effect due to crack in a beam between bending and axial vibrations was studied in [8] through an excitation in the axial direction by a shaker, which was used as a detection method for the crack. Through the shaft center locus and frequency domain graphs the response analysis were performed on a cracked shaft in [9] and they opined that the deep crack only had appreciable effect on responses. Experiments were conducted on a rotating shaft in [10], in which the crack was generated as a slot as well as a fatigue crack. The mathematical model-based estimation technique was utilized in frequency domain for the crack detection, localization and sizing.

Both crack and misalignment were investigated by frequency spectrum through a test rig data. The crack was developed by joining two shafts by the welding. Different types of cracks (fatigue crack, slit and welded joint) were investigated in [11, 12] and he opined that the fatigue crack was the most representative to mimic real life crack behavior in responses. With the help of change in the shaft slope information, two cracks location and its sizing were performed in [13] using an experimental setup. Cracks were fabricated using a hack-saw. The shaft was excited by means of an external sine-sweep exciter and the measurements were acquired using a laser vibrometer. Cracks were identified by means of crack probability functions.

The concept of directional-spectrum (or full-spectrum) is comparatively recent and has been evolved in previous three decades; however, its application is still uncommon. Directional-spectrum plots were used for identifying various faults in rotor systems [14–17]. These plots are useful as they have knowledge regarding the phase correlation between vibration patterns from diverse transducers. In one platform, a directional-spectrum graph depicts specific frequency constituents of rotor orbit that are in the same or opposite sense in regards to the direction of shaft rotation. In authors' earlier work, directional-spectrum plots were obtained using complex fast Fourier transforms [18, 19]. Model-based identification algorithms were developed in [20] for the parameter estimation in cracked rotors. The parame-

ters identified using the algorithms were: stiffness reduction in regards to the fatigue crack, coefficients of forces due to the crack switching, disc unbalance and its phase angle, and viscous damping. These algorithms were also numerically tested with responses simulated from a corresponding mathematical model. The inputs to these identification algorithms were obtained from time domain responses, Whereas, in [18, 19], the directional-spectrum signal processing technique was used to obtain the forward and reverse whirling force and response coefficients. These coefficients were then used as inputs to model-based identification algorithms. Very few attempts have been made on experimental investigation of breathing crack and hardly any work based on directional-spectrum, except briefly in [21] and the present work is more elaborate extension of the work, which requires worth more investigation especially on the estimation of the crack and other rotor parameters. This motivates us to perform extensive experimental identification of fatigue crack parameters in rotating condition through directional-spectrum analysis. Complex and interesting dynamical behavior has been observed in the nonlinear cracked rotor system. [22] studied the nonlinear response of cracked rotor and provided the phase diagrams indicative of crack diagnosis and control. Phase plots of the cracked rotor were generated with a parallel programming platform. A rotor crack with switching motion was modelled by [23] as a nonlinear variation of rotor stiffness with time. The cracked rotor was supported on sliding bearings and was modelled using nonlinear oil-film forces. An interesting phenomenon called the "eye of chaos" was discovered in the system, which arose due to bifurcation sequences. The crack nonlinearity has a characteristic "eye of chaos", arising from the bifurcation sequences. The dynamics of the cracked rotor are influenced by the crack parameters, namely, the angle and depth, as well as the oil film viscous parameter.

In this experimental work, a fatigue crack was generated artificially in a shaft. The loading is a bending fatigue in a 3-point fixture. Crack parameters are identified in frequency domain and for this purpose directional-spectrum plots have been used. All the inputs to the identification algorithm are obtained from responses measured from the experimental setup. From these identification algorithms, the following parameters are estimated: coefficients of the crack force, the viscous damping coefficient, the disc unbalance and its phase angle, and the additive stiffness due to fatigue crack. The content of the present work is now mentioned. A brief review of the identification algorithm of cracks is provided in Section 2. Whereas, in Section 3, the propagation of fatigue crack, and the fabrication and assembly of the test rig are elaborated. In Sections 4 and 5, acquisition of experimental responses and signal processing of these measured signals are discussed in detail. Finally, in Section 6, directional-spectrum plots and experimental identification of fatigue crack forces are discussed. The additive stiffness due to the occurrence of crack, along with the residual unbalance and the viscous damping has also been identified. Section 7 concludes the present work.

2. Crack identification algorithms

In the present study a rotor model with a fatigue crack is considered for mathematical model-based identification algorithm based on weight dominance so that equations remain linear. Fatigue cracks give rise to forward as well as reverse whirl at various harmonics of rotor spin frequency. Hence, the crack force has been modelled in a series form with various harmonics (forward as well as reverse) with its amplitude and frequencies. Equations of motion are documented in [18, 19], however, modified regression equations of identification algorithms are elaborated here for completeness, which is suitable for the present experimental investigation. For the identification of crack additive stiffness, disc unbalance, and viscous damping, the regression equation is written as,

$$\mathbf{A}_1\mathbf{x}_1 = \mathbf{b}_1 \qquad \text{with} \quad \mathbf{x}_{1(3\times1)} = \begin{bmatrix} c & e\mathrm{e}^{\mathrm{j}\beta} & \Delta k_{22} \end{bmatrix}^T, \tag{1}$$

$$\mathbf{A}_{1((2n+1)\times3)} = \begin{bmatrix} \mathrm{j}\,(-n\omega)\,r_{-n} & 0 & -w_x p_{-n} \\ \vdots & \vdots & \vdots \\ \mathrm{j}\,(-\omega)\,r_{-1} & 0 & -w_x p_{-1} \\ 0 & 0 & -w_x p_0 \\ \mathrm{j}(\omega) r_1 & -m\omega^2 e^{\mathrm{j}\beta} & -w_x p_1 \\ \mathrm{j}(2\omega) r_2 & 0 & -w_x p_2 \\ \vdots & \vdots & \vdots \\ \mathrm{j}\,(n\omega)\,r_n & 0 & -w_x p_n \end{bmatrix};$$

$$\mathbf{b}_{1((2n+1)\times1)} = \begin{Bmatrix} \left(n^2\omega^2 m - k_0\right) r_{-n} \\ \vdots \\ \left(\omega^2 m - k_0\right) r_{-1} \\ -k_0 r_0 \\ \left(\omega^2 m - k_0\right) r_1 \\ \left(4\omega^2 m - k_0\right) r_2 \\ \vdots \\ \left(n^2\omega^2 m - k_0\right) r_n \end{Bmatrix}.$$

In this regression equation, $\mathbf{A}_1$ is a regression matrix, $\mathbf{b}_1$ is an intercept, and $\mathbf{x}_1$ is the vector containing unknown parameters. Symbols used are defined as: the mass of the rotor as m, the intact shaft stiffness as k_0, the viscous damping as c, the eccentricity due to disc unbalance as e, the phase angle due to unbalance as β, the additive stiffness due to crack as Δk_{22}, the spin speed of the shaft as ω, w_y is the static defection of the shaft, p is the crack force coefficient, the complex

displacement as $r = x + \mathrm{j}y$, where p represent crack force frequency constituents and r represents displacement frequency constituents. Subscripts of variables p and r represent harmonics (*positive*: forward whirl and *negative*: backward whirl from directional-spectrum responses), the displacement frequency constituents are obtained from measured data and crack force frequency constituents are estimated from identification algorithm described in this section along with other unknown system parameters, and n is the number of harmonics considered (both the forward and backward). The size of the vectors and matrices is indicated in subscript within the bracket. On splitting the real and imaginary components, Eqn. (1) can be rewritten as follows.

$$\mathbf{A}_1^r \mathbf{x}_1^r - \mathbf{A}_1^i \mathbf{x}_1^i = \mathbf{b}_1^r \tag{2}$$

and

$$\mathbf{A}_1^i \mathbf{x}_1^r + \mathbf{A}_1^r \mathbf{x}_1^i = \mathbf{b}_1^r. \tag{3}$$

Superscripts r and i refer respectively to the real and imaginary portions. Eqn. (2) and Eqn. (3) can be combined in a matrix equation as follows.

$$\begin{bmatrix} \mathbf{A}_1^r & -\mathbf{A}_1^i \\ \mathbf{A}_1^i & \mathbf{A}_1^r \end{bmatrix}_{(4n+2)\times 6} \begin{Bmatrix} \mathbf{x}_1^r \\ \mathbf{x}_1^i \end{Bmatrix}_{(6\times 1)} = \begin{Bmatrix} \mathbf{b}_1^r \\ \mathbf{b}_1^i \end{Bmatrix}_{(4n+2)\times 1}. \tag{4}$$

The following row elements in the unknown vector $\left\lfloor \mathbf{x}_1^r \quad \mathbf{x}_1^i \right\rfloor_{(6\times 1)}^T$ are zero, i.e. $\mathbf{x}_1^i(4,1) = 0$ and $\mathbf{x}_1^i(6,1) = 0$. Corresponding to these row elements, the column elements in the regression matrix can also be eliminated. Thus,

$$\begin{aligned} &\mathbf{A}_1^r(1,4), \ldots, \mathbf{A}_1^r((2n+1),4) = 0; \quad \mathbf{A}_1^i((2n+1),4), \ldots, \mathbf{A}_1^r((4n+2),4) = 0; \\ &\mathbf{A}_1^r(1,6), \ldots, \mathbf{A}_1^r((2n+1),6) = 0; \quad \mathbf{A}_1^i((2n+1),6), \ldots, \mathbf{A}_1^r((4n+2),6) = 0. \end{aligned} \tag{5}$$

The resulting matrix equation is written as follows

$$\mathbf{A'}_{1((4n+2)\times 4)} \mathbf{x'}_{1(4\times 1)} = \mathbf{b'}_{1((4n+2)\times 1)} \quad \text{with} \quad \mathbf{x'}_1 = \left\lfloor c \;\; e\cos\beta \;\; \Delta k_{22} \;\; e\sin\beta \right\rfloor^T. \tag{6}$$

The above regression equation is utilized for obtaining the crack, damping and unbalance variables in a rotor system.

Estimation of crack forces:

As noted earlier, the force due to switching of crack contains superposition of force components at multiple harmonics of the spin speed. The coefficients of these various force components can be identified and identification algorithms for crack force terms are now described. The regression matrix is written as [18, 19]

$$\mathbf{A}_{2((2n+1)\times(2n+3))} = \begin{bmatrix} \mathbf{D}_1 & \mathbf{D}_2 \end{bmatrix} \tag{7}$$

where,

$$\mathbf{D}_1 = \begin{bmatrix} \mathrm{j}(-n\omega)r_{-n} & 0 & -w_x & 0 & 0 & 0 & 0 \\ \vdots & \vdots & \vdots & \vdots & \vdots & \vdots & \vdots \\ \mathrm{j}(-\omega)r_{-1} & 0 & 0 & 0 & 0 & 0 & -w_x \\ 0 & 0 & 0 & 0 & 0 & 0 & 0 \\ \mathrm{j}(\omega)r_1 & -m\omega^2 e^{\mathrm{j}\beta} & 0 & 0 & 0 & 0 & 0 \\ \mathrm{j}(2\omega)r_2 & 0 & 0 & 0 & 0 & 0 & 0 \\ \vdots & \vdots & \vdots & \vdots & \vdots & \vdots & \vdots \\ \mathrm{j}(n\omega)r_n & 0 & 0 & 0 & 0 & 0 & 0 \end{bmatrix},$$

$$\mathbf{D}_2 = \begin{bmatrix} 0 & 0 & 0 & 0 & 0 & 0 & 0 & 0 \\ \vdots & \vdots & \vdots & \vdots & \vdots & \vdots & \vdots & \vdots \\ 0 & 0 & 0 & 0 & 0 & 0 & 0 & 0 \\ -w_x & 0 & 0 & 0 & 0 & 0 & 0 & 0 \\ 0 & -w_x & 0 & 0 & 0 & 0 & 0 & 0 \\ 0 & 0 & -w_x & 0 & 0 & 0 & 0 & 0 \\ \vdots & \vdots & \vdots & \vdots & \vdots & \vdots & \vdots & \vdots \\ 0 & 0 & 0 & 0 & 0 & 0 & 0 & -w_x \end{bmatrix},$$

$$\mathbf{x}_{2((2n+3)\times 1)} = \begin{Bmatrix} c \\ e \\ \Delta k_{22} p_{-n} \\ \vdots \\ \Delta k_{22} p_{-1} \\ \Delta k_{22} p_0 \\ \Delta k_{22} p_1 \\ \Delta k_{22} p_2 \\ \vdots \\ \Delta k_{22} p_n \end{Bmatrix}; \qquad \mathbf{b}_{1((2n+1)\times 1)} = \begin{Bmatrix} \left(n^2\omega^2 m - k_0\right) r_{-n} \\ \vdots \\ \left(\omega^2 m - k_0\right) r_{-1} \\ -k_0 r_0 \\ \left(\omega^2 m - k_0\right) r_1 \\ \left(4\omega^2 m - k_0\right) r_2 \\ \vdots \\ \left(n^2\omega^2 m - k_0\right) r_n \end{Bmatrix}.$$

Separating Eqn. (7) in to the real and imaginary parts, as described in previous section, and representing as the matrix equation, it gives,

$$\mathbf{A}'_{2((4n+2)\times(2n+4))}\mathbf{x}'_{2((2n+4)\times 1)} = \mathbf{b}'_{2((2n+4)\times 1)} \tag{8}$$

with,

$$\mathbf{x}'_2 = \left\lfloor c \; e\cos\beta \; e\sin\beta \; \Delta k_{22} p_{-n} \; \ldots \; \Delta k_{22} p_{-1} \; \Delta k_{22} p_0 \; \Delta k_{22} p_1 \; \ldots \; \Delta k_{22} p_n \right\rfloor^T. \tag{9}$$

In the above equations, the number of harmonic components considered in the algorithm is general and varies from 1 to n for forward components, and -1 to $-n$ for reverse components in steps of 1. In this paper, the above described algorithms will be tested with experimental data as their input. The overall experimental procedure is shown as a flowchart in Fig. 1 and individual steps are elaborately described in subsequent sections.

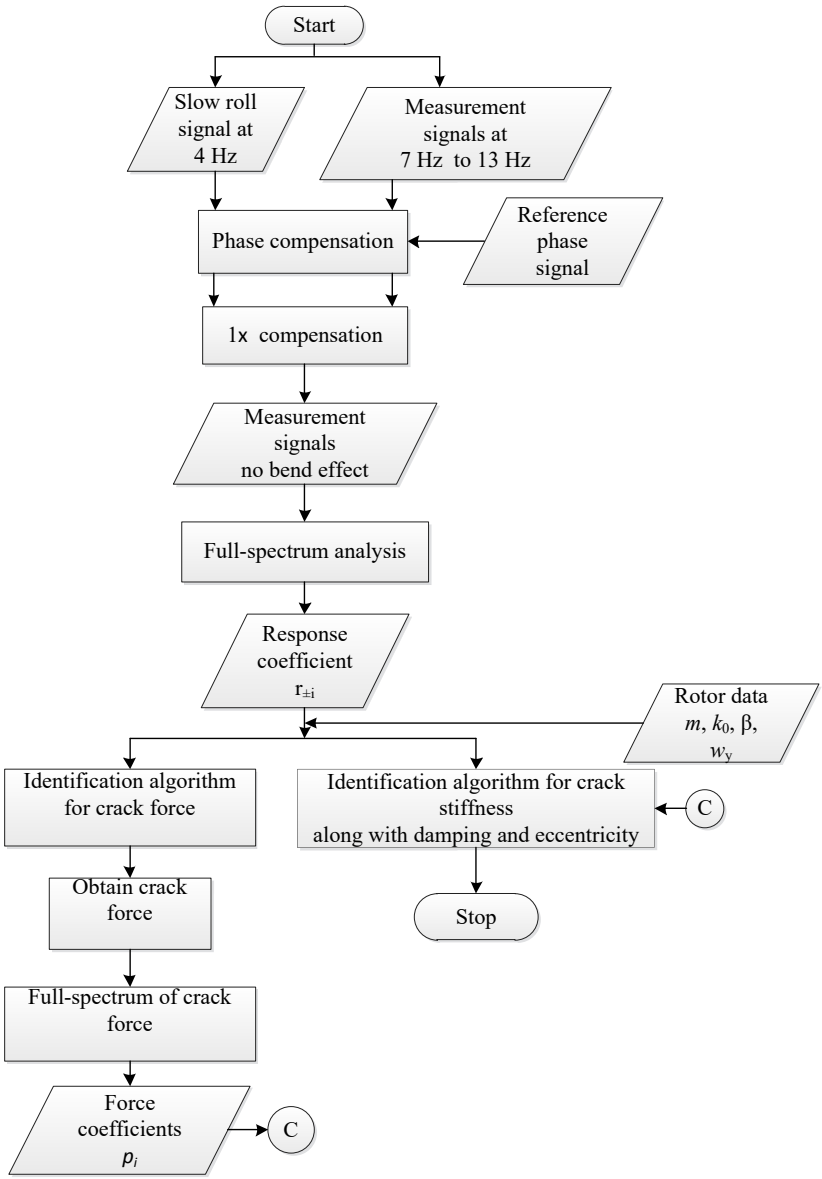

Fig. 1. Flowchart showing experimental procedure for the crack force identification

3. Experimental setup

An experimental setup was assembled for the model-based crack identification. The experimental setup includes a mild steel shaft in which a fatigue crack is developed. A disc was mounted at an offset position on the shaft, which in turn was mounted on ball bearing supports on either ends. A flexible coupling links the rotor shaft with that of the motor. A squirrel cage induction motor regulated by a variable frequency drive (VFD) was selected as the rotor drive. For measurements, vibration signals were measured using eddy-current type non-contact displacement sensors. A photo-sensitive sensor was also used for measuring a reference signal, which helps in calculating phase lag of measured signals. A line diagram for the experimental layout is shown in Fig. 2. Part numbers are mentioned in the figure (all dimensions are in mm) and the corresponding lists of parts are tabulated in Table 1.

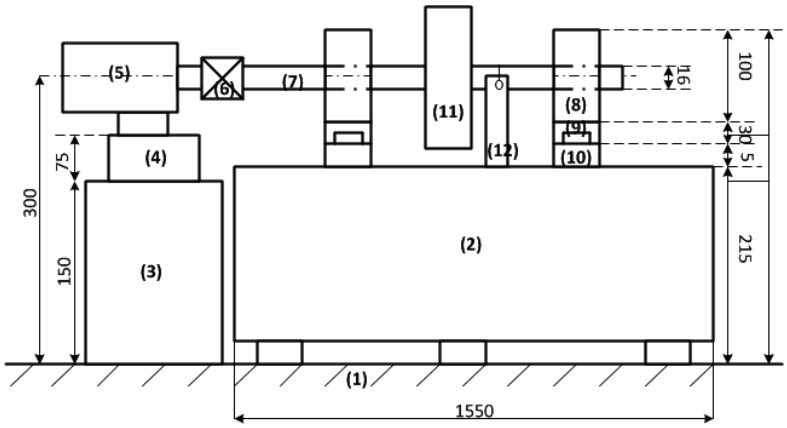

Fig. 2. Plan for experimental setup of a cracked rotor (ref. Table 1)

Table 1.

List of parts of the experimental rotor setup

Part No.	Part Name	Part No.	Part Name
(1)	Bed	(7)	Shaft with crack
(2)	Rotor bed	(8)	Bearing holder ×2
(3)	Motor base	(9)	Bearing holder base ×2
(4)	Additional motor base	(10)	Shims ×4
(5)	Motor	(11)	Disk
(6)	Coupling	(12)	Sensor holder at crack location

Primary objectives of the experimentation were to study the switching/ breathing mechanism of a fatigue crack, and for the estimation of crack and remaining unidentified variables. For this, the measured experimental data were processed and

used as an input to the model-based identification algorithms described in Eq. (6) and Eq. (8). In this section, preparation of a rotor shaft, generation of fatigue crack in the shaft, and data sensing and acquisition are discussed.

3.1. Preparation of rotor shaft

A mild steel rotor shaft of 15.8 mm diameter and 545 mm length was prepared by turning operation and then grounded. A notch was machined using a horizontal milling machine with a 45° angle-milling cutter. The notch is located axially at 225 mm from one of the shaft end as shown in Fig. 3. The generation of fatigue crack is now discussed.

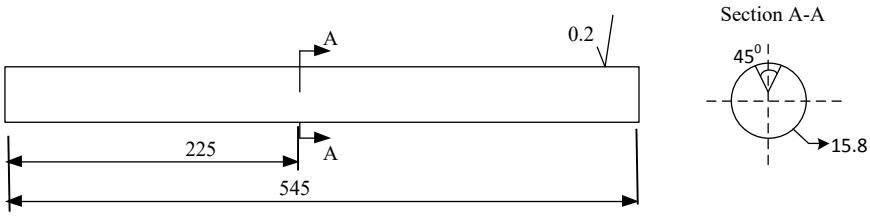

Fig. 3. A shaft with a V-notch

3.2. Development of a shaft crack

When shaft material is impressed upon repeated forcing, the fatigue crack develops confined to a small area of the section, and its tendency is to advance to a larger area of the section. One of the objectives in this work was to initiate a crack (i.e., fatigue pre-crack) from the tip of the V-notch (cavity) in a rotor shaft, which can be used for rotor crack identification. Also, hardly any standards are available for the fatigue testing of plain round shafts. In this regard, the development of crack due to repeated loading in the shaft is a challenging process.

The fatigue crack is expected to initiate at the notch position of the shaft specimen, as it has a maximum local stress (stress concentration). Hence, the specimen shaft with V-notch was subjected to cyclic stress using a 100 kN capacity universal tensile testing machine with a three-point bending fixture. The specimen could also be cyclically loaded in its axial direction. In both cases, the crack initiation by fatigue failure at the notch is expected in Mode I. It is defined as the opening mode and the principal deformation is transverse to the crack front [22].

3.2.1. Principle of Operation

Notched shaft specimens were supported on two precision machine fixed anvils (Fig. 4) of a defined radius (10 mm). The force was applied centrally so that the shaft was subjected to three-point bending with fatigue load. The support beam

was graduated lengthwise in metric units for accurate positioning of anvils equally spaced relative to the central line. Adjustable specimen stops were provided so that the specimen could be loaded quickly and accurately positioned on the lower anvils.

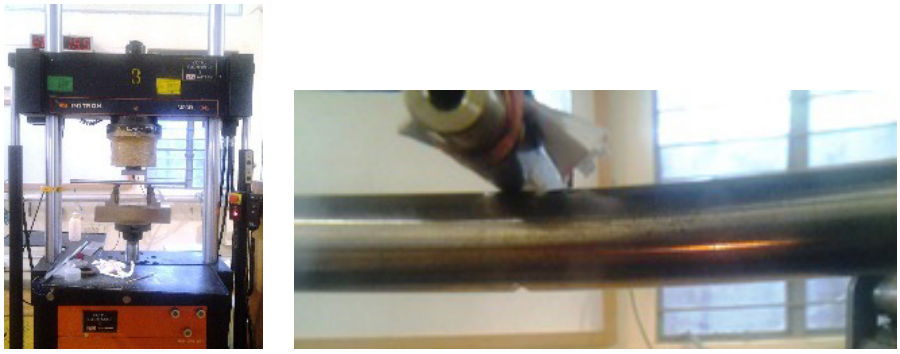

(a) (b)

Fig. 4. (a) Specimen in universal tensile machine; (b) shaft with V-notch during fatigue loading

3.2.2. Methodology for Indication of Initiated Crack

In the fatigue loading, the component fails at stress values, which are far less than the ultimate tensile stress and yield stress values for the material under uniform tension. Hence, for the fatigue testing, the shaft specimen was subjected a cyclic load whose maximum value was well below the yield stress value of the specimen material. Once maximum ($P_{\max}$), mean (P_{mean}) and minimum values ($P_{\min}$) for the cyclic fatigue loading were chosen; the shaft specimen was subjected to this load and the crack initiation was expected after a certain number of cycles. In order to monitor for the crack initiation, the following methodology was conceived. Experimentally determined calibration curves relate the displacement per unit load to the crack length for different specimens. The calibration relationship is generally given as [24],

$$EB\bar{v}/P = F\left(\bar{a}/\bar{w}\right), \tag{10}$$

where E is the Young's modulus, B is the specimen thickness, $\bar{w}$ is the specimen width, $\bar{v}$ is the displacement, P is the load, $F\left(\bar{a}/\bar{w}\right)$ is the function of $\bar{a}/\bar{w}$ for single-edge-cracked specimens and dependent on the specimen geometry, where $\bar{a}$ is the initiated crack length and $\bar{w}$ is the specimen width. Hence, it can be seen that with constant E and B, the load versus displacement curve (or $\bar{v}/P$) is dependent on the function $F\left(\bar{a}/\bar{w}\right)$. Hence, with increase in the crack length $\bar{a}$ for a given loading P, the displacement (i.e., positional amplitude) $\bar{v}$ is also expected to increase. Also, the slope of the load versus displacement curve corresponds to the stiffness of the notch section of the shaft with any crack. Hence, the stiffness or the slope of this

curve is expected to decrease with increase in the displacement. Thus, a change (increase) of 12% of the initial value of the positional amplitude was chosen as the suitable indicator for initiation of the fatigue crack from the notch tip.

3.2.3. Static Loading Three-Point Bending Test

A static 3-point transverse loading was initially performed to find the shaft specimen yield strength and its Young's modulus (measure of stiffness). This is used to calculate the maximum and minimum values of the applied fatigue loads. The shaft was mounted with point contacts on two machine-fixed anvils of defined radius. The load was applied centrally at the third point of contact. The notch location was central to the support span and opposite the location of load application. The specimen was continuously deflected with a fixed strain increment of 0.5 mm/min and the corresponding loads were measured. A load versus deflection curve was plotted from the corresponding data (Fig. 5a). It can be observed from the figure that when the load reaches a value of 8 kN, the specimen undergoes a noticeable plastic deformation.

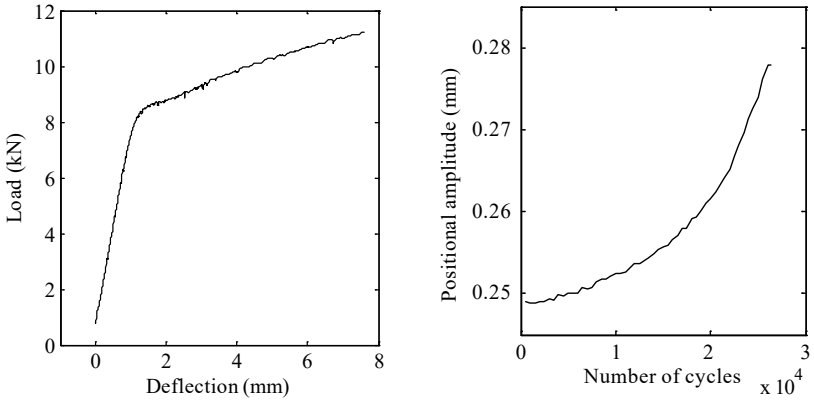

(a) (b)

Fig. 5. (a) Load versus deflection curve for the shaft specimen with notch; (b) cyclic 3-point transverse load test depicting the count of cycles versus the positional amplitude

3.2.4. Cyclic Loading Three-Point Bending

Based on observed load at yield point, a cyclic fatigue load with $P_{\max} = 6$ kN and $P_{\min} = 1.8$ kN (i.e., corresponding to a stress quotient of $R = 0.3$) was selected as the fatigue load to be applied to the shaft using a hydraulic-servo actuator. The shaft was mounted as described above in a common 3-point transverse loading arrangement. The test configuration is specified in Table 2. For an applied number of fatigue cycles, the displacement value, i.e. the positional amplitude of the shaft

Table 2.

Fatigue loading three-point bending test configuration

Machine type and capacity	Ultimate tensile testing machine, 100 kN
Test method	Three point bending test
Operating frequency	10 Hz
Stress ratio, R	0.3 at 25°C
Compression	6 kN to 1.8 kN
Support span	140 mm

at the notch location was measured. The plot of count of the load repetition versus the positional amplitude is shown in Fig. 5b.

The initial value of the positional amplitude measured at the notch section of the shaft at the beginning of repetitive forcing was 0.2491 mm. The shaft specimen was subjected to fatigue loading for 26400 cycles. The final value of the positional amplitude after completion of cycles of fatigue loading was measured as 0.2779 mm. This corresponds to a 12% increase in the positional amplitude at the notch section. This is indicative of the initiation of the fatigue crack at the notch.

As an alternative means to confirm the crack initiation, a liquid dye penetrant was used to perform Dye Penetrant Inspection (DPI). It is based on capillary action of the dye where it initially penetrates into discontinuities of the fatigue crack. The excess dye on the surface is then wiped out. During successive cycles of loading, the dye comes out from the ends of the cavity. This indicates the presence of any discontinuities, which in this case is a fatigue crack. In this manner, a fatigue crack was initiated and verified, as shown in Fig. 6. Also, optical microscope was used to observe the fatigue crack. A progressive width fatigue crack in the range of micrometers was observed with 10× and 20× magnifications. Fig. 7a shows the

(a) (b)

Fig. 6. Fatigue crack developed in the notched shaft by cyclic loading: (a) a view parallel to the crack front, (b) a view perpendicular to the crack front

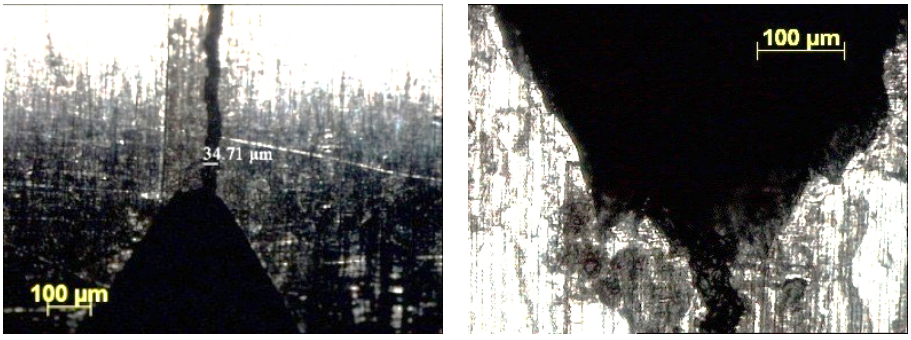

(a) (b)

Fig. 7. Optical microscope pictures showing a progressive fatigue crack and the notch: (a) the crack growth from V-notch, (b) the V-notch

fatigue crack initiated from the V-notch with a width of 34.71 µm and Fig. 7b shows the V-notch at a magnification of 20×.

However, as an after-effect of fatigue crack initiation, the shaft was bent with a maximum deflection of 0.4 mm at the center. This necessitates the removal of bow effect from all subsequently measured vibration data. This will be elaborated in a latter section on processing of measured signals. The shaft with initiated fatigue crack was subsequently assembled with other components of the cracked rotor test setup. The final assembly of the cracked rotor test setup together with the data acquisition equipment is shown in Fig. 8. Now, details of the data acquisition equipment are discussed.

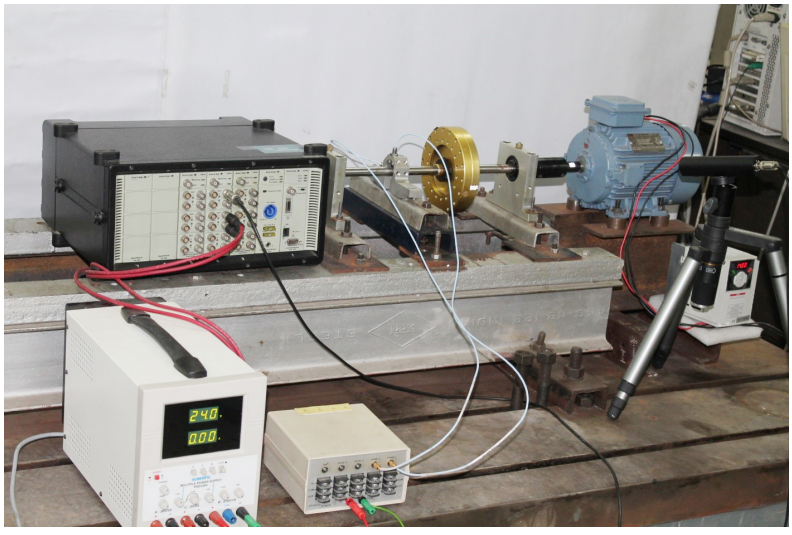

Fig. 8. A bird-eye view of cracked rotor test setup

4. Data acquisition and procedure for experimentation

This section provides the details of data acquisition equipment used and the experimental procedure.

4.1. Data acquisition equipment

For measuring shaft displacement in two orthogonal directions, eddy-current displacement probe (Bently-Nevada make) was used (Fig. 9). For the measurement of spin speed and for acquiring a reference signal, a photoelectric tachometer probe (Model MM-0024, Brüel & Kjaer make) was used. A reflective tape attached on the motor shaft surface acts as an external reference mark. The probe was safely placed 300 mm from the object. Pulse Analyser sound and vibration analysis software was used for data acquisition.

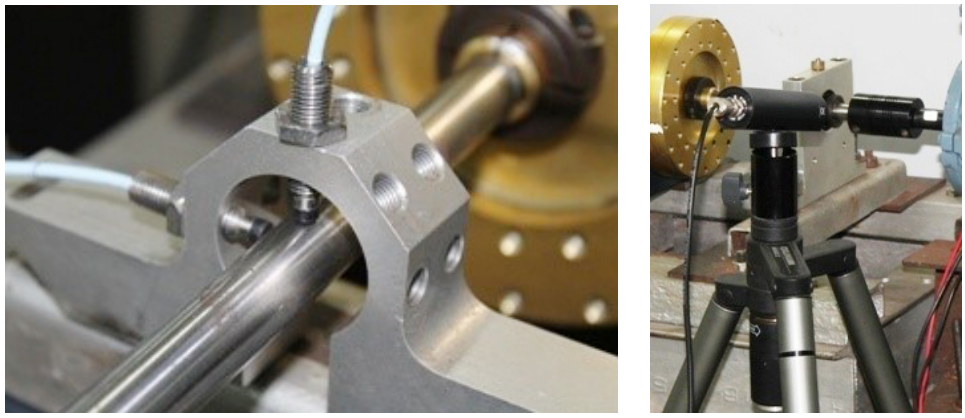

(a) (b)

Fig. 9. (a) Eddy current proximity probes for displacement measurement in two orthogonal transverse directions; (b) the measurement of the speed and the reference signal

4.2. Procedure for experimentation

The rotor in the cracked shaft setup is subjected to dynamic forces, one due to the disc unbalance and the other because of switching/ breathing process of a fatigue crack. The excitation force frequency because of the disc unbalance comprises of the rotor spin frequency (i.e., 1×). Whereas, excitation force because of the fatigue crack comprises of several frequency constituents, which are harmonics (forward and reverse) of the rotor spin speed (i.e., −5×, −3×, 1×, 7×, etc.).

In the procedure for experimentation, the free vibration tests are initially carried out to obtain the cracked rotor system natural frequencies. Based on free vibration tests, the *spin-speed range* is selected. Then, displacement responses were acquired

for each of the spin-speeds. These are then transformed into frequency domain by use of the directional-spectrum transformation (i.e., complex-FFT). These displacement responses in frequency domain are then processed for phase and slow-roll compensations. Finally, they are input to the identification algorithms. In the following section, the data acquisition of measurement signals and their processing are discussed.

4.3. Post-processing of acquired responses

As mentioned earlier, the foremost challenge in the post-processing of the acquired displacement responses was the removal of the effect of shaft bow (which inadvertently comes during the generation of fatigue crack). It is known that a shaft bend force mimics similar to unbalance force but with a difference that the former has a magnitude independent of the spin speed of the shaft. This section discusses the procedure of compensation for the shaft bow in measured responses at a particular speed, based on the *slow-roll response* (i.e., displacement response acquired at a very slow speed).

Prior to 1× *compensation* the phase-shifting [26] is performed. The slow-roll and displacement responses are post-processed such that both responses are acquired from the same reference mark, which corresponds to a pulse in the reference signal, i.e. their relative phase angle at any given instant becomes zero. This is termed as *phase shifting*. The phase shifting of the signals is done in time domain prior to directional-spectrum transformation (for obtaining magnitude and phase information of 1×frequency component) [14] and 1× compensation.

5. Experimental measurements

In this section, the acquisition of measurement signals from the test setup and the processing of the signals are described.

5.1. Free vibration tests

The cracked rotor system is subjected to free vibration testing using an impact load on its various components. Accelerometers were mounted on the bearing and disc locations, and vibration responses due to impact at different locations were measured. Frequency spectrum plots (i.e., FFT plots) provided its natural frequencies. The bandwidth of the FFT was chosen so as to accommodate few initial natural frequencies of the test setup. The tests were repeated and natural frequencies corresponding to the rotor system were obtained. Fig. 10 shows the free vibration response plots. During free vibration tests, the fatigue crack effect was expected to be negligibly small due to small magnitude of impact on the structure. Also, only the effect of notch as an open crack contributes to the measured natural frequency.

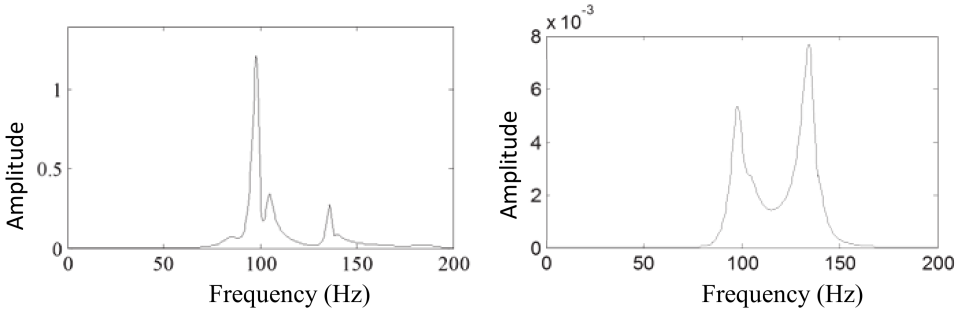

(a) (b)

Fig. 10. Frequency response function while the impact position on the rotor disc from: (a) accelerometer on the bearing, (b) accelerometer on the shaft

5.1.1. Inferences from the impact test

Fundamental natural frequency of the simply supported cracked rotor shaft with a disc mass was 98 Hz. This relates to nearly the fundamental forward critical speed of the test setup. Natural frequencies corresponding to other impact locations were: (i) for the rotor base and the foundation 100 Hz, (ii) for the bearing 136 Hz and (iii) for the coupling 141 Hz. Based on these free vibration test results, the spin-speed range was chosen well below these natural frequencies to avoid critical speeds and/or resonance conditions. This also ensures safety from the failure due to crack propagation during experimentation.

5.2. Acquisition of displacement responses

For acquiring displacement responses, the spin-speed range for response acquisition was chosen as 7 Hz to 14 Hz in steps of 1 Hz. From the results of the free vibration test, the first natural frequency of the cracked rotor system is observed at 98 Hz. Hence, for the cracked rotor setup under study, critical speed corresponds to ($14 \times 7 = 98$ Hz) seventh harmonic of the crack forcing frequency. From the definition of slow-roll, 5 Hz (300 rpm) is chosen as the spin-speed for slow-roll response, while spin-speeds from 7 Hz (420 rpm) to 13 Hz (780 rpm) are chosen as the spin-speed range for acquiring displacement response for the crack identification.

Displacement responses from eddy current probes in two orthogonal directions are obtained as depicted in Fig. 11. The reference signal (or key phasor signal) for phase is also shown along with the displacement response. Similar procedure was followed for other spin-speeds.

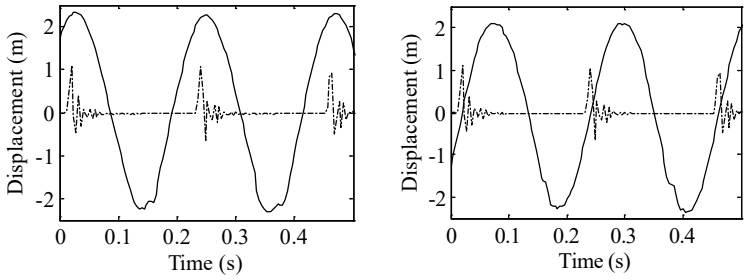

Fig. 11. Displacement time history (solid line) at 5 Hz rotor speed with corresponding the phase signal (dashed line): (a) in the horizontal sensor positions, (b) vertical sensor positions

5.3. Phase shifting of slow-roll and displacement responses

One of displacement response and one slow-roll response are shown in Fig. 12. It shows that that at initial capturing of two responses are independent and at different locations with respect to a fixed position on the rotor, which represents as a spike.

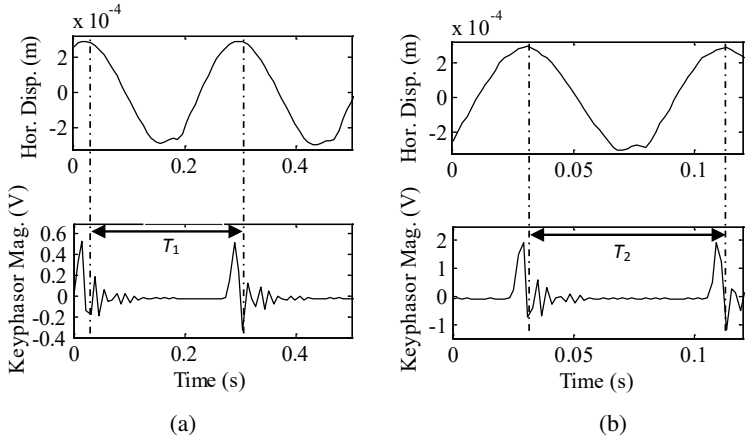

Fig. 12. (a) Slow-roll displacement (top) and phase signal at 4 Hz (bottom); (b) displacement (top) and phase signal at 13 Hz (bottom)

Before subtraction for 1× *compensation*, both the displacement response and the slow-roll response are processed so as to result that: i) both the responses are acquired from the 0° phase angle of the reference mark at $t = 0$, ii) the displacement response is interpolated in order to have same number of sample points as that of slow-roll response. Now, the magnitude and phase information of slow-roll response can be subtracted from that of the displacement response. Such phase-shifted responses plotted for one time-period are shown in Fig. 13.

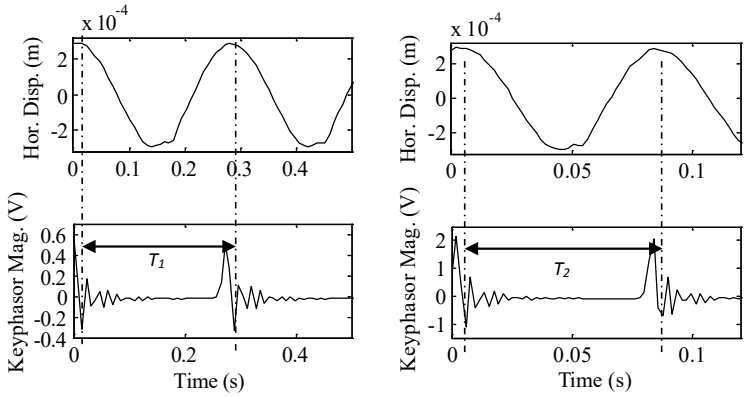

Fig. 13. (a) Phase-shifted slow-roll response; (b) phase-shifted displacement response at 13 Hz

5.4. The 1× compensation for removal of shaft bow

After the phase shifting, directional-spectrum plots of phase-shifted responses are obtained. Such responses are acquired for spin-speeds range of 7 Hz (420 rpm) to 13 Hz (780 rpm) with slow-roll speed of 5 Hz (300 rpm). Then, corresponding to 1× frequency component of directional-spectrum, the magnitude and phase of slow-roll response is subtracted from the magnitude and phase information of displacement response. This is known as the 1× *compensation* and it results in slow-roll compensated directional-spectrum plots.

The compensated directional-spectrum plots are in frequency domain. Hence, their Fourier coefficients correspond to *displacement coefficients* of measurement signals without the effect of shaft bow. Displacement coefficients of measurement signals at slow-roll and 13 Hz are shown in Fig. 14a and Fig. 14b, respectively.

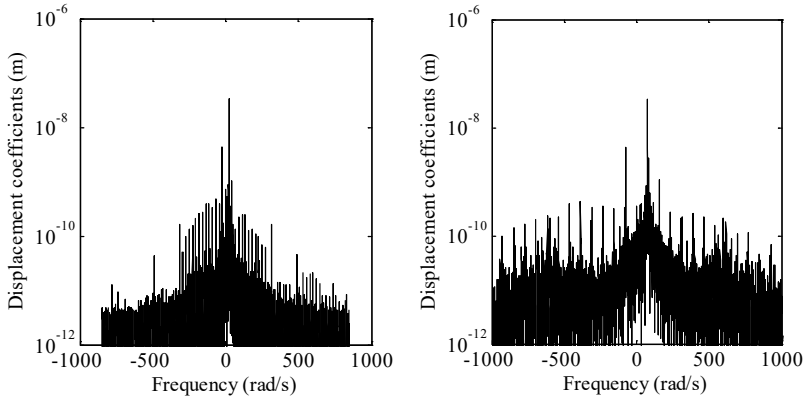

Fig. 14. Directional-spectrum graph depicting displacement coefficients at: (a) the slow-roll; (b) 13 Hz speed with 1× removed

6. Experimental crack identification

In this section, estimation of crack and other unknown system parameters by means of identification algorithms is presented. Some of rotor system parameters are through measurements: disc mass $m = 2$ kg, from an impact test the fundamental natural frequency of test rotor $\omega_{nf} = 98$ Hz, so the shaft stiffness with slit is $k = \omega_{nf}^2 m = 7.6 \times 10^5$ N/m, the slow-roll speed as 5 Hz, and the measurement speeds 7 Hz to 13 Hz in steps of 1 Hz.

Displacement coefficients will be chosen as inputs and the identification algorithms (described in Eqn. (1) through Eqn. (8)) will be tested, for three different sets of measurement spin speed ranges.

6.1. Identification of crack force

Directional-spectrum transformation of slow roll responses is obtained in which the magnitude (i.e., Fourier coefficients) of harmonic components correspond to displacements. Displacement coefficients are obtained for the spin-speed range of 7 Hz to 13 Hz. Three examples for range of measurement spin speeds are chosen for testing of identification algorithms, as shown in Table 3.

Table 3.

Measurement spin speed ranges

Example	Measurement spin speed range
I	7 Hz to 10 Hz with frequency interval of 1 Hz
II	11 Hz to 13 Hz with frequency interval of 1 Hz
III	7 Hz to 13 Hz with frequency interval of 1 Hz

Displacement coefficients which are obtained are then input to the identification algorithm, which estimates the crack force (Eq. (7)). The known rotor system parameters are also used as an input to identification algorithms.

Then, the estimates of $\Delta k_{22} p_i$ are obtained as elaborated in [18]. These estimates contain information about the force due to fatigue crack. It is to be noted that p_i also corresponds to the magnitude (i.e., Fourier coefficients) of the crack force in frequency domain. Hence, these estimates provide the crack forces. For Example I, identified crack forces in two orthogonal directions are depicted in Fig. 15. Also, estimated forces for Example II are depicted in Fig. 16, and estimated force for Example III is provided in Fig. 17. In the estimation equation Eqn. (2), i is substituted with the forward and backward harmonics; $-11\times$, $-10\times$, ..., $-1\times$, 0, $1\times$, $2\times$, ..., $11\times$.

From the identified crack forces, it is observed that in the crack front direction, it is lopsided about the average value. Whereas, the force is symmetrical in an orthogonal direction in which crack is absent. For example, it can be observed that, for Example III, the force bound is -60 N to 40 N. On other hand, the crack force

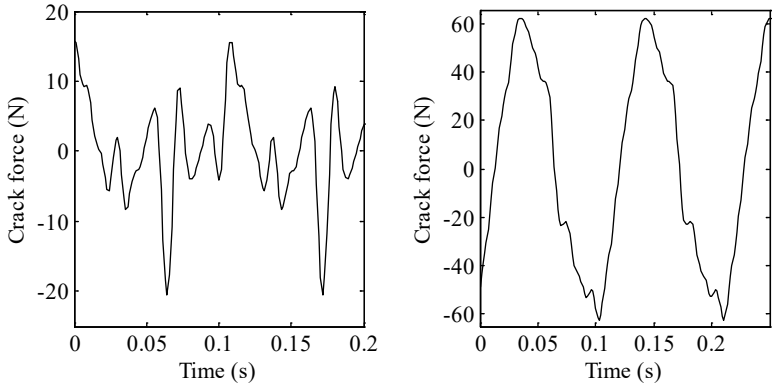

Fig. 15. Variation of crack force for measurement Example I at a spin speed of 7 Hz: (a) towards the crack front; (b) orthogonal to the crack front

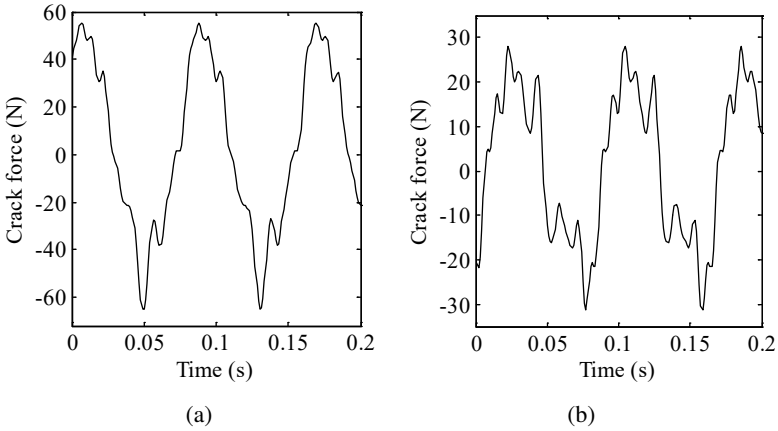

Fig. 16. Variation of crack force for measurement Example II at a spin speed of 11 Hz: (a) towards the crack front; (b) orthogonal to the crack front

in the orthogonal direction is symmetric about the average value and the bound is −40 N to 40 N.

While the crack is in bottom orientation of the shaft then it is entirely open because of the gravity load, whereas when it is at top orientation of the shaft then it is entirely closed, and in remaining orientations it is partly closed. It results in an asymmetrical crack force in the direction of the crack front. Wherein, a symmetrical crack force is observed in orthogonal to the crack front.

Directional-spectrum plots of force of fatigue crack, as shown in Fig. 15 through Fig. 16, are obtained, which give *force coefficients*. Force coefficients at a measurement speed of 13 Hz are shown in Fig. 17. These force coefficients are obtained similarly for all measurement speeds from 7 Hz to 13 Hz.

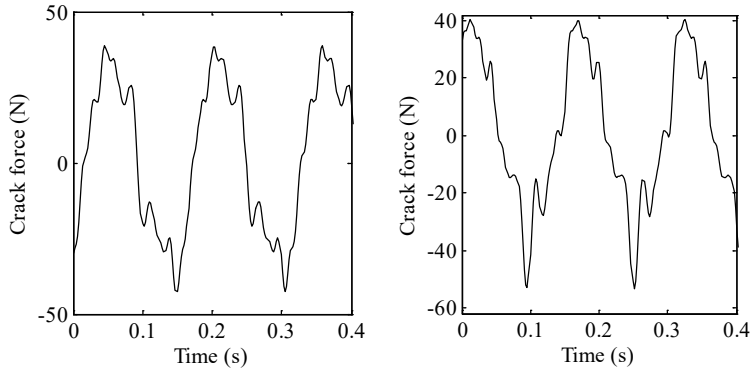

Fig. 17. Variation of crack force for measurement Example III at a spin speed of 13 Hz: (a) towards the crack front; (b) orthogonal to the crack front

6.2. Identification of crack, unbalance, and viscous damping

Now, force frequency constituents and displacement frequency constituents are both used as an input to the identification algorithm described in Eqn. (1). This identification algorithm estimates the additive stiffness, the disc eccentricity along with its phase, and the shaft viscous damping. The additive stiffness parameter is an indicator of the crack and the disc eccentricity causes unbalance. Displacement coefficients (Fig. 14) and system parameters (given in beginning of Section 6) along with force coefficients (Fig. 18) are used as an input to the identification algorithm to estimate the above said parameters. Experimentally estimated parameters for the cracked shaft system are tabulated in Table 4.

Table 4.

Parameter estimates from the identification algorithm

Parameter	Estimates from Example I	Estimates from Example II	Estimates from Example III
Viscous damping, c	272 N·s/m	14 N·s/m	272 N·s/m
Disc eccentricity, e	0.042 mm	0.041 mm	0.042 mm
Phase angle	303.6°	315.6°	303.6°
Additive crack stiffness, Δk_{22}	3.56×10^4 N/m	3.99×10^4 N/m	3.56×10^4 N/m

Parameters estimated corresponding to measurement Example III (Table 3) are better, as they include measurements from Example I as well as Example II. Hence, the inferences are drawn from estimates of Example III.

The estimated additive crack stiffness (i.e., 3.56×10^3 N/m) with that of intact shaft stiffness (i.e., 7.6×10^5 N/m) can be compared. It is seen that, because of the introduction of a fatigue crack in the shaft, a 0.5% reduction in the intact shaft stiffness has been predicted. So, the stiffness of the cracked shaft is 7.56×10^5 N/m.

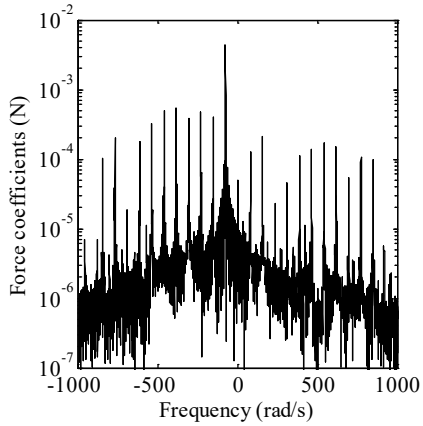

Fig. 18. Directional-spectrum graph depicting force coefficients at a speed of 13 Hz

The ratio of intact shaft stiffness to the shaft stiffness with the crack can be related to the ratio of diameter of intact shaft to the equivalent diameter of shaft with the crack. It is given as $(k_{\text{intact}}/k_{\text{cracked}}) = \left(d^4_{\text{intact}}/d^4_{\text{crack}}\right)$. The equivalent diameter of shaft with crack is then obtained as 15.78 mm. As the intact shaft diameter chosen for the experiment was 15.8 mm, this corresponds to 0.12% reduction in the intact shaft diameter due to the crack growth. The effect of the notch machined to the shaft has already been considered in the shaft stiffness, obtained based on free vibration test results. A notch represents an open crack and cannot have any contribution in the variation of stiffness. Hence, the percentage reduction in stiffness corresponds to the fatigue crack alone.

6.3. Inferences from experimental results

The acquired displacement responses are processed prior to their further use in the identification algorithm. The slow-roll response was acquired at a rotor spin-speed of 5 Hz. The measurement spin-speeds range was chosen between 7 Hz to 13 Hz. The *phase shifting*, followed with 1× *waveform compensation* of the slow-roll response was performed to eliminate the effect of bend in the shaft. Then, forces due to the switching mechanism of fatigue crack were experimentally estimated. These estimated forces are unsymmetrical in their force magnitude, when obtained the direction of crack. This can be inferred as model-based identification of the of fatigue crack in the rotor shaft. Then, directional-spectrum plots of crack forces and displacement responses were obtained, which provided force frequency constituents and displacement frequency constituents, respectively. These frequency constituents are fed as an input to the identification algorithm, which estimates the crack parameter. Also, the unbalance and viscous damping are identified. From the estimates obtained, it is observed that, because of occurrence of crack, the stiffness of intact shaft reduces by 0.5%.

7. Conclusions

A fatigue crack was experimentally introduced by three-point bending in a mild steel shaft. Since hardly any standards were available for the fatigue testing of plain round shafts, a trial and error method was used along with the dye penetrant inspection to observe the initiation of crack. The shaft was assembled in a rotor-bearing-coupling experimental set-up, for the identification of crack along with unknown system parameters. The natural frequency obtained for the cracked rotor from impact test was 98 Hz. For measurements in the dynamic condition, spin-speeds were chosen well below critical speed (7 Hz to 13 Hz), and independent measurements were obtained at constant spin speed. Two displacement signals in orthogonal directions and one key-phasor signal for the phase were measured. The constant phase of the displacement responses was ensured as measurement speeds did not cross any critical speed.

An experimental set up was developed to study the fatigue crack behavior in a rotor assembly. A fatigue crack was experimentally introduced by three-point bending in a mild steel shaft. The rotor assembly with the cracked shaft was used for data acquisition and processing of acquired displacement responses. Procedures for the experimental crack identification were elaborately developed, which include: acquisition of slow-roll as well as displacement responses, phase shifting of displacement responses by using an external reference signal; and 1× compensation of displacement responses in directional-spectrum frequency domain using a slow-roll response. This removes the effect of shaft bend from the measured responses. Then, force frequency constituents and displacement frequency constituents are obtained using directional-spectrum plots of estimated force responses and slow-roll compensated displacement responses. These coefficients are obtained from processing of the acquired signals. They are then taken as an input to the identification algorithm. Fault parameters of crack stiffness and disc eccentricity were estimated experimentally, along with system damping. The estimated force responses clearly identify the occurrence of crack in the rotor system. The parameter estimates also indicate the reduction in shaft stiffness due to occurrence of crack. Implementation of present methodology in real rotor crack would be interesting. In future work, the crack can be modelled using non-linear or stochastic methods, and parameter estimation can be carried out [27].

Manuscript received by Editorial Board, May 22, 2019;
final version, July 31, 2019.

References

[1] Y. Ishida. Cracked rotors: Industrial machine case histories and nonlinear effects shown by a simple Jeffcott rotor. *Mechanical Systems and Signal Processing*, 22(4):805–817, 2008. doi: 10.1016/j.ymssp.2007.11.005.

[2] G. Sabnavis, R.G. Kirk, M. Kasarda, and D. Quinn. Cracked shaft detection and diagnostics: a literature review. *The Shock and Vibration Digest*, 36(4):287–296, 2004. doi: 10.1177/0583102404045439.

[3] N. Dharmaraju, R.Tiwari, and S. Talukdar. Identification of an open crack model in a beam based on force-response measurements. *Computers & Structures*, 82(2-3):167–179, 2003. doi: 10.1016/j.compstruc.2003.10.006.

[4] A.S. Sekhar. Crack identification in a rotor system: a model-based approach. *Journal of Sound and Vibration*, 270(4-5):887–902, 2004. doi: 10.1016/S0022-460X(03)00637-0.

[5] A.C. Chaselevris and C.A. Papodopoulos. Experimental detection of an early developed crack in rotor-bearing system using an AMB. *Third International Conference of Engineering against Failure*, June 26–28, 2013, Kos, Greece.

[6] P. Gudmundson. The dynamic behaviour of slender structures with cross-sectional cracks. *Journal of the Mechanics and Physics of Solids*, 31(4):329–345, 1983. doi: 10.1016/0022-5096(83)90003-0.

[7] C.A. Papadopoulos and A.D. Dimarogonas. Stability of the cracked rotors in the coupled vibration mode. *Journal of Vibration, Acoustics, Stress, and Reliability in Design*, 110(3):356–359, 1988.

[8] A.K. Darpe, K. Gupta, and A. Chawla. Experimental investigations of the response of a cracked rotor to periodic axial excitation. *Journal of Sound and Vibration*, 260(2):265–286, 2003. doi: 10.1016/S0022-460X(02)00944-6.

[9] T. Zhou, Z. Sun, J. Xu, and W. Han. Experimental analysis of cracked rotor. *Journal of Dynamic systems, Measurement, and Control*, 127(3):313–320, 2005. doi: 10.1115/1.1978908.

[10] P. Pennacchi, N. Bachschmid, and A. Vania. A model-based identification method of transverse cracks in rotating shafts suitable for industrial machines. *Mechanical Systems and Signal Processing*, 20(8):2112–2147, 2006. doi: 10.1016/j.ymssp.2005.04.005.

[11] J.K. Sinha. Higher order spectra for crack and misalignment identification in the shaft of a rotating machine. *Structural Health Monitoring*, 6(4):325–334, 2007. doi: 10.1177/1475921707082309.

[12] Z. Cai. *Vibration diagnostics of elastic shafts with a transverse crack*. Master Thesis, Faculty of Computing, Health and Science, Edith Cowan University, Perth, Australia 2011.

[13] S.K. Singh and R. Tiwari. Detection and localization of multiple cracks in a shaft system: An experimental investigation. *Measurement*, 53:182–193, 2014. doi: 10.1016/j.measurement.2014.03.028.

[14] D. Southwick. Using full spectrum plots: Part 2. *Orbit*, 15(2):10–16. 1994.

[15] P. Goldman and A. Muszynska. Application of full spectrum to rotating machinery diagnostics. *Orbit*, 17–21, 1999.

[16] J. Tuma, and J. Bilos. Fluid induced instability of rotor systems with journal bearings. *Engineering Mechanics*, 14(1-2):69–80, 2007.

[17] T.H. Patel and A.K. Darpe. Application of full spectrum analysis for rotor fault diagnosis. In: *IUTAM Symposium on Emerging Trends in Rotor Dynamics*, 1011:535–545, 2011.

[18] C. Shravankumar and R. Tiwari. Detection of fatigue crack in a rotor system using full-spectrum based estimation. *Sadhana*, 41(2):239–251, 2016. doi: 10.1007/s12046-015-0452-9.

[19] C. Shravankumar and R. Tiwari. Model-based crack identification using full-spectrum. In *Proceedings of the ASME 2013 Gas Turbine India Conference*, Bangalore, Karnataka, India, December 5–6, 2013. doi: 10.1115/GTINDIA2013-3756.

[20] C. Shravankumar and R. Tiwari. Identification of stiffness and periodic breathing forces of a transverse switching crack in a Laval rotor. *Fatigue and Fracture of Engineering Materials and Structures*, 36(3):254–269, 2012. doi: 10.1111/j.1460-2695.2012.01718.x.

[21] C. Shravankumar, R. Tiwari, and A. Mahibalan. Experimental identification of rotor crack forces. In: *Proceedings of the 9th IFToMM International Conference on Rotor Dynamics*: pp. 361–371, 2015. doi: 10.1007/978-3-319-06590-8_28.

[22] X.B. Rao, Y.D. Chu, Y.X. Chang, J.G. Zhang, and Y.P. Tian. Dynamics of a cracked rotor system with oil-film force in parameter space. *Nonlinear Dynamics*, 88(4):2347–2357, 2017. doi: 10.1007/s11071-017-3381-9.

[23] B.C. Wen and Y.B.Wang. Theoretical research, calculation and experiments of cracked shaft dynamical responses. In *Proceedings of International Conference on Vibration in Rotating Machinery*, pp. 473–478, London, UK, 1988.

[24] Prashant Kumar. *Elements of Fracture Mechanics*. Wheeler Publishing, New Delhi, 1999.

[25] M.G. Maalouf. Slow-speed: vibration signal analysis. *Orbit*, 27(2):4–16, 2007.

[26] R. Tiwari. *Rotor Systems: Analysis and Identification*. CRC Press, USA, 2017. doi: 10.1201/9781315230962.

[27] L.G.G. Villani, S. da Siva, and A. Cunha Jr. Damage detection in uncertain nonlinear systems based on stochastic Volterra series. *Mechanical Systems and Signal Processing*, 125:288–310, 2019. doi: 10.1016/j.ymssp.2018.07.028.